

Whole-body multispectral photoacoustic imaging of adult zebrafish

NA HUANG,^{1,4} HENG GUO,^{1,4} WEIZHI QI,^{1,4} ZHIWEI ZHANG,³ JIAN RONG,^{1,2}
ZHEN YUAN,³ WEI GE,³ HUABEI JIANG,^{1,2} AND LEI XI^{1,2,*}

¹*School of Physical Electronics, University of Electronic Science and Technology of China, Chengdu, Sichuan, China*

²*Center for Information in Biomedicine, University of Electronic Science and Technology of China, Sichuan, China*

³*Faculty of Health Sciences, University of Macau, Macau, China*

⁴*These authors contributed equally to this work*

*xilei1985@uestc.edu.cn

Abstract: The zebrafish, an ideal vertebrate for studying developmental biology and genetics, is increasingly being used to understand human diseases, due to its high similarity to the human genome and its optical transparency during embryonic stages. Once the zebrafish has fully developed, especially wild-type breeds, conventional optical imaging techniques have difficulty in imaging the internal organs and structures with sufficient resolution and penetration depth. Even with established mutant lines that remain transparent throughout their life cycle, it is still challenging for purely optical imaging modalities to visualize the organs of juvenile and adult zebrafish at a micro-scale spatial resolution. In this work, we developed a non-invasive three-dimensional photoacoustic imaging platform with an optimized illumination pattern and a cylindrical-scanning-based data collection system to image entire zebrafish with micro-scale resolutions of 80 μm and 600 μm in the lateral and axial directions, respectively. In addition, we employed a multispectral strategy that utilized excitation wavelengths from 690 nm to 930 nm to statistically quantify the relative optical absorption spectrum of major organs.

©2016 Optical Society of America

OCIS codes: (170.5120) Photoacoustic imaging; (170.6960) Tomography.

References and links

1. J. H. Postlethwait, Y. L. Yan, M. A. Gates, S. Horne, A. Amores, A. Brownlie, A. Donovan, E. S. Egan, A. Force, Z. Gong, C. Goutel, A. Fritz, R. Kelsh, E. Knapik, E. Liao, B. Paw, D. Ransom, A. Singer, M. Thomson, T. S. Abduljabbar, P. Yelick, D. Beier, J. S. Joly, D. Larhammar, F. Rosa, M. Westerfield, L. I. Zon, S. L. Johnson, and W. S. Talbot, "Vertebrate genome evolution and the zebrafish gene map," *Nat. Genet.* **18**(4), 345–349 (1998).
2. D. M. Langenau, D. Traver, A. A. Ferrando, J. L. Kutok, J. C. Aster, J. P. Kanki, S. Lin, E. Prochownik, N. S. Trede, L. I. Zon, and A. T. Look, "Myc-induced T cell leukemia in transgenic zebrafish," *Science* **299**(5608), 887–890 (2003).
3. J. Hove, "In vivo biofluid dynamic imaging in the developing Zebrafish. *Birth Defects Res,*" *C Embryo* **72**, 277–289 (2004).
4. K. D. Poss, L. G. Wilson, and M. T. Keating, "Heart regeneration in Zebrafish," *Science* **298**(5601), 2188–2190 (2002).
5. J. T. Shin and M. C. Fishman, "From zebrafish to human: modular medical models," *Annu. Rev. Genomics Hum. Genet.* **3**(1), 311–340 (2002).
6. C. Zanella, M. Campana, B. Rizzi, C. Melani, G. Sanguinetti, P. Bourguine, K. Mikula, N. Peyrieras, and A. Sarti, "Cells segmentation from 3-D confocal images of early zebrafish embryogenesis," *IEEE Trans. Image Process.* **19**(3), 770–781 (2010).
7. O. Bandmann and E. A. Burton, "Genetic zebrafish models of neurodegenerative diseases," *Neurobiol. Dis.* **40**(1), 58–65 (2010).
8. J. F. Amatrudda and E. E. Patton, "Genetic models of cancer in zebrafish," *Int. Rev. Cell Mol. Biol.* **271**, 1–34 (2008).
9. M. Kamali, L. J. Day, D. H. Brooks, X. Zhou, and D. M. O'Malley, "Automated identification of neurons in 3D confocal datasets from zebrafish brainstem," *J. Microsc.* **233**(1), 114–131 (2009).

10. H. Lin, A. Chekkoury, M. Omar, T. Schmitt-Manderback, B. Koberstein-Schwarz, T. Mappes, H. Lopez-Schier, D. Razansky, and V. Ntziachristos, "Selective plane illumination optical and optoacoustic microscopy for postembryonic imaging," *Laser Photonics Rev.* **9**(5), L29–L34 (2015).
11. A. Bassi, L. Fieramonti, C. D'Andrea, M. Mione, and G. Valentini, "In vivo label-free three-dimensional imaging of zebrafish vasculature with optical projection tomography," *J. Biomed. Opt.* **16**(10), 100502 (2011).
12. S. Isogai, M. Horiguchi, and B. M. Weinstein, "The vascular anatomy of the developing zebrafish: an atlas of embryonic and early larval development," *Dev. Biol.* **230**(2), 278–301 (2001).
13. R. M. White, A. Sessa, C. Burke, T. Bowman, J. LeBlanc, C. Ceol, C. Bourque, M. Dovey, W. Goessling, C. E. Burns, and L. I. Zon, "Transparent adult zebrafish as a tool for in vivo transplantation analysis," *Cell Stem Cell* **2**(2), 183–189 (2008).
14. S. Kabli, S. He, H. P. Spaink, A. Hurlstone, E. S. Jagalska, H. J. De Groot, and A. Alia, "In vivo magnetic resonance imaging to detect malignant melanoma in adult zebrafish," *Zebrafish* **7**(2), 143–148 (2010).
15. E. Seo, J. H. Lim, S. J. Seo, and S. J. Lee, "Whole-body imaging of a hypercholesterolemic female zebrafish by using synchrotron X-ray micro-CT," *Zebrafish* **12**(1), 11–20 (2015).
16. W. Goessling, T. E. North, and L. I. Zon, "Ultrasound biomicroscopy permits in vivo characterization of zebrafish liver tumors," *Nat. Methods* **4**(7), 551–553 (2007).
17. P. Beard, "Biomedical photoacoustic imaging," *Interface Focus* **1**(4), 602–631 (2011).
18. L. V. Wang and S. Hu, "Photoacoustic tomography: in vivo imaging from organelles to organs," *Science* **335**(6075), 1458–1462 (2012).
19. L. Xi, S. R. Grobmyer, L. Wu, R. Chen, G. Zhou, L. G. Gutwein, J. Sun, W. Liao, Q. Zhou, H. Xie, and H. Jiang, "Evaluation of breast tumor margins in vivo with intraoperative photoacoustic imaging," *Opt. Express* **20**(8), 8726–8731 (2012).
20. L. Xi and H. Jiang, "High resolution three-dimensional photoacoustic imaging of human finger joints in vivo," *Appl. Phys. Lett.* **107**(6), 063701 (2015).
21. R. A. Kruger, C. M. Kuzmiak, R. B. Lam, D. R. Reinecke, S. P. Del Rio, and D. Steed, "Dedicated 3D photoacoustic breast imaging," *Med. Phys.* **40**(11), 113301 (2013).
22. S. Ye, R. Yang, J. Xiong, K. K. Shung, Q. Zhou, C. Li, and Q. Ren, "Label-free imaging of zebrafish larvae in vivo by photoacoustic microscopy," *Biomed. Opt. Express* **3**(2), 360–365 (2012).
23. R. Ma, M. Distel, X. L. Deán-Ben, V. Ntziachristos, and D. Razansky, "Non-invasive whole-body imaging of adult zebrafish with optoacoustic tomography," *Phys. Med. Biol.* **57**(22), 7227–7237 (2012).
24. S. P. Mattison, R. L. Shelton, R. T. Maxson, and B. E. Applegate, "Continuous real-time photoacoustic demodulation via field programmable gate array for dynamic imaging of zebrafish cardiac cycle," *Biomed. Opt. Express* **4**(8), 1451–1463 (2013).
25. M. Liu, N. Schmitzer, M. G. Sandrian, B. Zabihian, B. Hermann, W. Salvenmoser, D. Meyer, and W. Drexler, "In vivo three dimensional dual wavelength photoacoustic tomography imaging of the far red fluorescent protein E2-Crimson expressed in adult zebrafish," *Biomed. Opt. Express* **4**(10), 1846–1855 (2013).
26. J. Park, T. M. Cummins, M. Harrison, J. Lee, Q. Zhou, C. L. Lien, and K. K. Shung, "High frequency photoacoustic imaging for in vivo visualizing blood flow of zebrafish heart," *Opt. Express* **21**(12), 14636–14642 (2013).
27. D. Razansky, M. Distel, C. Vinegoni, R. Ma, N. Perrimon, R. Köster, and V. Ntziachristos, "Multispectral opto-acoustic tomography of deep-seated fluorescent proteins in vivo," *Nat. Photonics* **3**(7), 412–417 (2009).
28. L. Xi, C. Song, and H. Jiang, "Confocal photoacoustic microscopy using a single multifunctional lens," *Opt. Lett.* **39**(11), 3328–3331 (2014).
29. M. Fonseca, B. Zeqiri, P. C. Beard, and B. T. Cox, "Characterisation of a phantom for multiwavelength quantitative photoacoustic imaging," *Phys. Med. Biol.* **61**(13), 4950–4973 (2016).
30. L. Xi, X. Li, L. Yao, S. Grobmyer, and H. Jiang, "Design and evaluation of a hybrid photoacoustic tomography and diffuse optical tomography system for breast cancer detection," *Med. Phys.* **39**(5), 2584–2594 (2012).
31. M. Omar, D. Soliman, J. Gateau, and V. Ntziachristos, "Ultrawideband reflection-mode optoacoustic mesoscopy," *Opt. Lett.* **39**(13), 3911–3914 (2014).
32. G. Li, L. Li, L. Zhu, J. Xia, and L. V. Wang, "Multiview Hilbert transformation for full-view photoacoustic computed tomography using a linear array," *J. Biomed. Opt.* **20**(6), 066010 (2015).

1. Introduction

In the past two decades, the zebrafish has attracted increasing attention from the biological, medical, and pharmaceutical communities as an ideal model for studying the evolution, development, diseases, and treatment of vertebrates [1–4]. Due to their similarity with the genome and early development of humans, the zebrafish is now widely used to explore gene expression, the nervous and circulatory systems, cardiovascular diseases and cancers in humans [5–8]. In the embryonic stage, the zebrafish is transparent. This feature allows conventional optical imaging modalities, such as epifluorescence microscopy, confocal microscopy, multiphoton microscopy (MPM), selective plane illumination microscopy (SPIM), and optical coherence tomography (OCT), to image organs/structures of interest at an ultrahigh spatial

resolution [9–12]. However, due to the rapid growth of zebrafish, purely optical techniques have difficulty in visualizing organs and structures inside the zebrafish in juvenile and adult stages with sufficient resolution and penetration depth. Recently, White et al. investigated a mutant type of zebrafish that remains transparent throughout its life cycle [13]. Using a fluorescence confocal microscope, the authors achieved an ultrahigh resolution of 5 μm and a maximal imaging depth of 88 μm . Although successful in tracking single cells in the kidney marrow space, challenges remain in studying the innermost internal tissues that are typically located more than 1 mm beneath the surface. Even by the use of two/multi-photon fluorescence microscopy, the penetration depth is limited to 1 mm, which is insufficient for visualizing deep tissues. In addition, optical microscopic techniques require the use of fluorescent tags to serve as external contrast sources [12, 13]. Apart from optical imaging modalities, magnetic resonance microimaging (μMRI), micro computed tomography (μCT), and ultrasound biomicroscopy, which use intrinsic contrast, have been successfully applied in zebrafish studies. Kabli et al. utilized a 17.6-T ultra-high magnetic field to realize the whole-body imaging of zebrafish in vivo with a high spatial resolution of 78 μm [14]. The authors successfully obtained detailed anatomical structures and clear morphological proton images of different organs by T2-weighted spin echo, and achieved rapid acquisition by using relaxation enhancement sequences [14]. However, in addition to the very high cost of the imaging equipment, μMRI is restricted to anatomical examination and it is difficult to derive functional parameters. μCT has the merits of being cost-efficient, yielding high resolution, and being extra sensitive to dense tissues, however it involves ionizing radiation and has low sensitivity to soft tissues [15]. Goessling et al. used ultrasound biomicroscopy to image liver tumors in adult zebrafish in vivo at spatial resolutions of 68.2 μm and 38.5 μm in the lateral and axial directions, respectively [16]. However, the low contrast and strong speckle artifacts of its ultrasound images prevents its extensive application.

Photoacoustic imaging (PAI), a hybrid imaging modality with rich optical contrast and high ultrasound resolution, shows great potential in various biological and medical applications such as gene expression, vasculature visualization, arthritis diagnosis, brain imaging, and cancer treatment [17–21]. Generally, there are two sub-modalities known as photoacoustic computed tomography (PACT) and photoacoustic microscopy (PAM). The spatial resolution of PACT varies from tens to hundreds of micrometers and the imaging depth ranges from millimeters to centimeters depending on the center frequency and bandwidth of the ultrasonic transducer. PAM has a higher resolution, from sub-micron to sub-millimeter, and the penetration depth is usually less than a centimeter [17, 18]. Several groups have successfully used PAM and PACT to study zebrafishes [22–27]. Li et al. developed a technique known as transmission optical resolution photoacoustic microscopy (ORPAM), which allows for the study of the microvasculature of zebrafish larvae at a lateral resolution of 6 μm [22]. Razansky and Ntziachristos successfully mapped the internal structures, organs, and labeled fluorescence probes of adult zebrafishes via PACT [23, 27]. Applegate and Zhou developed new acoustic detectors to study the zebrafish heart [24, 26]. Drexler et al. demonstrated the use of dual-wavelength photoacoustic imaging to track genetically expressed fluorescent proteins in the exocrine pancreas of adult zebrafish [25]. In our study, we developed a multispectral cylindrical-scanning photoacoustic imaging system with optimized illumination to visualize all the internal organs and structures in the adult zebrafish. Through quantitative and statistical analyses of multispectral images excited via light wavelengths from 690 nm to 930 nm, we successfully obtained the absorbing spectrum of the major zebrafish organs, including the ovary, liver, spleen, kidney, stomach, and heart, which can be used to guide the selection of the optimal wavelength for specific organs.

2. Methods

2.1 System configuration

Figure 1 shows the schematic of system configurations. Briefly, a pulsed OPO laser (Surelite OPO, Continuum, CA) pumped by a Q-switched Nd:YAG laser (Surelite I-20, Continuum, CA) with a duration of 20 ns and a repetition rate of 20 Hz served as the photoacoustic excitation source. The output laser beam was uniformly split via three non-polarization beam splitters (BS014, Thorlabs Inc, NJ), then coupled into four optical fiber bundles with a core size of 3 mm though using four converging lenses. The output pulse energy of each bundle was 3.5 mJ. To form a homogeneous illumination pattern on the surface of zebrafish, the bundles were distributed symmetrically with a spacing angle of 90° to form a homogeneous illumination pattern on the sample surface as shown in Fig. 1. Generated wideband photoacoustic signals were collected by a cylindrically focused ultrasound transducer with 10 MHz center frequency, 9 mm aperture and 25.4 mm focal length. The transducer was mounted in the imaging interface and rotated 360° with a constant scanning step of 0.5° leading to a total number of 720 A-line photoacoustic signals for one two-dimensional (2D) scanning. After amplified by a pre-amplifier (5073PR, Olympus, MA), the photoacoustic signals were recorded via a 12 bits data acquisition card (NI-5124, National Instruments Corporation, TX) with a sampling rate of 50 MHz. To achieve three-dimensional (3D) imaging, the samples were mounted on a Z-axis step motor with a scanning interval of $300\ \mu\text{m}$. For anatomical and multispectral mapping, we selected 9 excitation wavelengths from 690 nm to 930 nm. The measured pulse energy on the sample surface was $2.8\ \text{mJ}/\text{cm}^2$ that was far below the American National Standards Institute (ANSI) safety limit of $22\ \text{mJ}/\text{cm}^2$. A reconstruction program developed based on delay&sum algorithm was used to rebuild the 2D photoacoustic images that were stacked to form a 3D image.

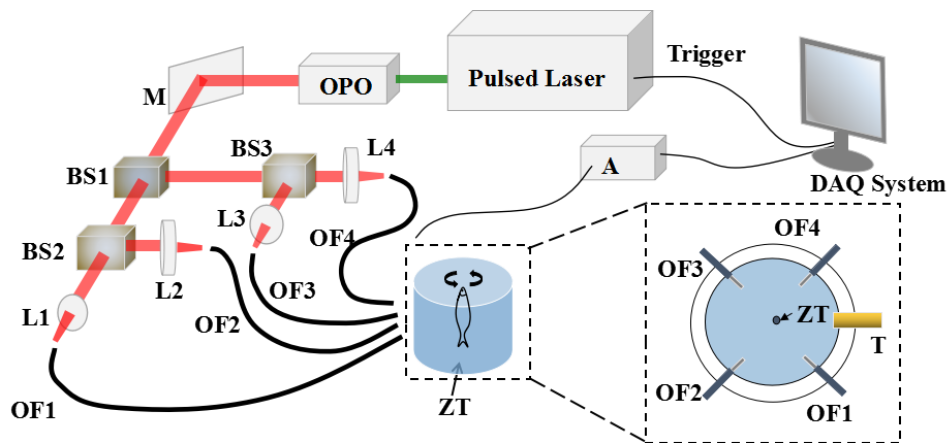


Fig. 1. Experimental configuration of photoacoustic imaging system. OPO: Optical Parametric Oscillator M: Mirror BS: Beam Splitter L: Lens A: Amplifier Z: Zebrafish T: Transducer OF: Optical Fiber.

2.2 Phantom preparation

In order to evaluate the performance of the system, a $7\ \mu\text{m}$ carbon fiber and tissue mimicking background phantom was prepared. India ink and intralipid were mixed to simulate an optical absorption coefficient of $0.01\ \text{mm}^{-1}$ and a reduced scattering coefficient of $1.0\ \text{mm}^{-1}$. The mixture was solidified by agarose and shaped through a hollow aluminum cylinder. Several carbon fibers were embedded in the tissue mimicking phantom and imaged. The imaged size of the carbon fibers were used to characterize the lateral and axial resolutions of the system.

2.3 Animal handling

Adult zebrafishes were anesthetized in a 0.1% tricaine solution and carefully immobilized in a solidified agarose holder except the head. After the experiments, zebrafish were fixed in the Bouin's fixative solution and stored in 70% alcohol solution. Fixed zebrafish were then embedded in paraffin sections and sliced at 5 μm thickness. All the slices were stained with hematoxylin and eosin and captured using a Nikon eclipse Ni microscope.

2.4 Data processing

For quantitative analysis, we manually segmented organs images, divided each organ into 4 sub-regions and then summed all data points in the sub-regions to calculate the relative optical absorbing coefficient of organs. Four independent groups of experiments were performed for statistical analysis and all data were summarized using means \pm standard error of the mean (SEM).

3. Results

To evaluate the effective imaging area of the proposed system, we scanned a tissue-mimicking phantom that contained carbon fibers over a large area. Figure 2(a) shows a 10 mm \times 10 mm 2D image in which no obvious distortion was observed. For spatial resolution evaluation, we selected the carbon fiber, as indicated by the dashed white line. Figures 2(b) and 2(c) show the lateral and axial profiles of the carbon fiber, respectively. We found that the full widths at half maximum (FWHM) were 80 μm and 600 μm , respectively, which represent the best lateral and axial resolutions of the system. Theoretically, the best axial resolution of the system is approximately 420 μm , which is slightly better than the experimental value [28]. The major reason for this difference is that the selected carbon fiber was not precisely positioned in the focal length of the transducer. Typically, for photoacoustic imaging systems utilizing cylindrical transducers, the axial resolution will slightly degrade when samples are placed outside the focal line. Furthermore, the accuracy of the Z-axial step motor is 50 μm , which may cause a discrepancy between the experimental and theoretical resolutions.

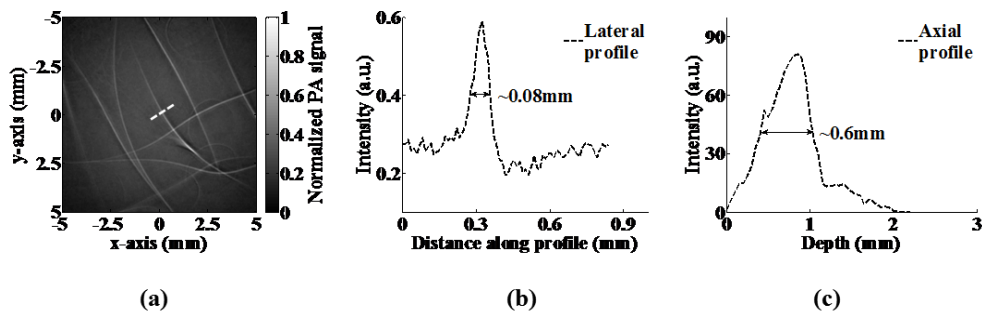


Fig. 2. (a) The reconstructed image of the carbon fibers. (b) Lateral profile of the selected carbon fiber. (c) Axial profile of the selected carbon fiber.

To carry out whole-body imaging, we performed 90 cross-sectional scans and stacked them to form a volumetric image. As shown in Fig. 3, two typical slices of the zebrafish head are compared with their corresponding histological sections. Besides the clear boundary and internal structures of the head, we can identify various organs and tissues, including the brain, heart, vertebrae, pharynx, hypobranchial musculature, musculature, and gill. Of these organs, the brain and heart are the most important for developing disease models to better understand associated human diseases.

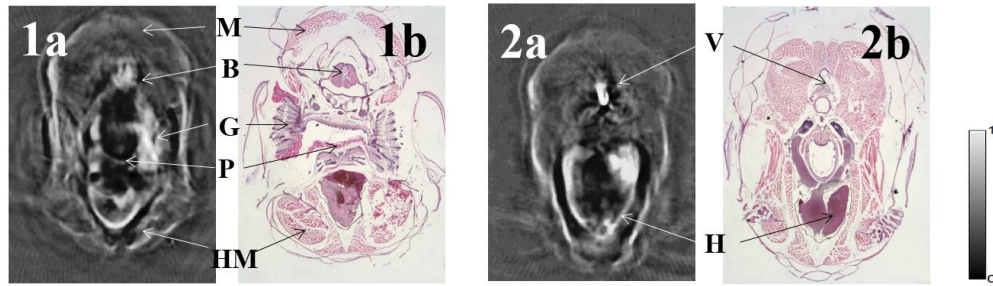


Fig. 3. Two selected PAT images of an adult (four-month-old) zebrafish head. B: Brain H: Heart V: Vertebrae P: Pharynx HM: Hypobranchial Musculature M: Musculature G: Gill.

In addition to the organs located in the head, we also successfully captured images of muscles, and the kidney, liver, stomach, swim bladder, spleen, and ovary in various positions, as shown in Fig. 4.

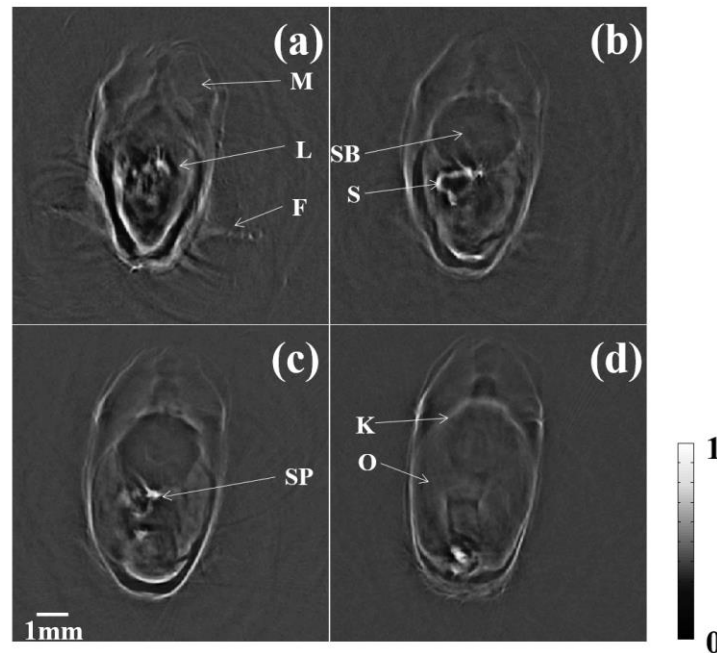


Fig. 4. Four typical anatomical slices of a zebrafish. M: muscle K: kidney L: liver S: stomach SB: swim bladder SP: spleen O: ovary F: fins ([Visualization 1](#)).

We chose four representative layers containing major organs for conducting multispectral imaging and quantitative analysis. From the results shown in Fig. 5, we can see that most organs revealed a distinct photoacoustic intensity under different excitation wavelengths. The optical absorptions of the major organs and tissues—the ovary, kidney, spleen, liver, heart, and muscle—decrease when the excitation wavelength increases. Interestingly, inside the head, we observed additional structures of the pharynx and slight changes in the photoacoustic intensity of the brain tissue with an increase in the excitation wavelength.

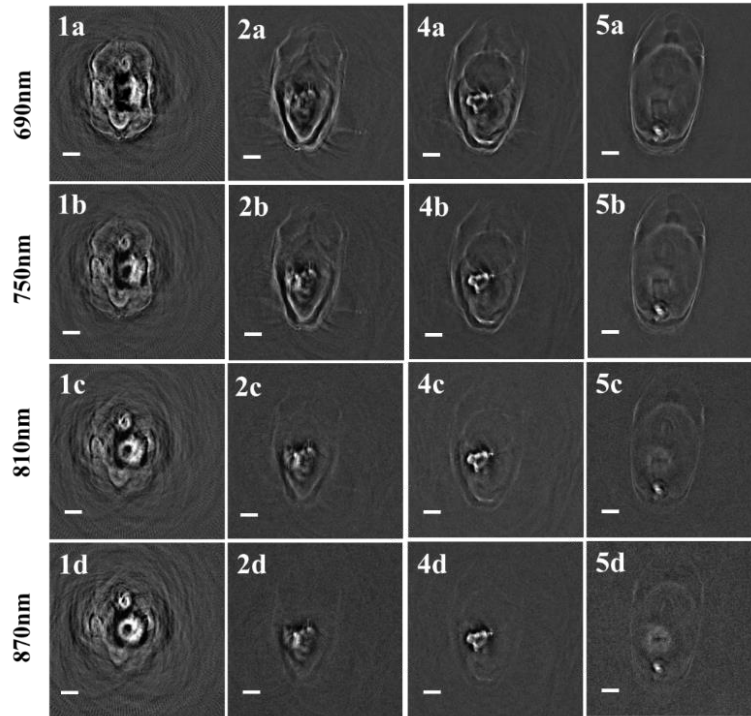


Fig. 5. Four typical multispectral images of an entire zebrafish.

The quantitative analyses of the typical organs shown in Fig. 6 indicates that: 1) the liver and spleen have the strongest optical absorption; 2) the kidney, heart, and stomach exhibit moderate optical absorption; and 3) the ovary has the weakest optical absorption. By utilizing the multispectral features of organs, we can select optimized wavelengths with the strongest light absorption for each of the organs.

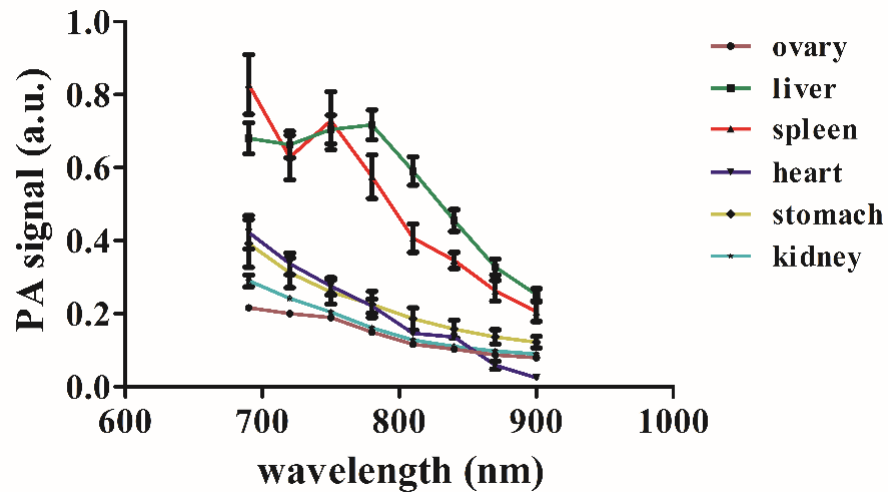


Fig. 6. Quantitative multispectral analysis of major organs.

4. Conclusion and discussion

In this work, we developed a non-invasive 3D photoacoustic imaging system with a homogeneous side-view light illumination delivered by multiple optical fiber bundles. The system's lateral and axial resolutions are 80 μm and 600 μm , respectively. We imaged adult zebrafish and were able to observe various organs and structures inside the intact body. To our knowledge, this is the first detailed study of zebrafish via multispectral photoacoustic imaging. Multispectral study enables the selection of the best wavelength for different organs and structures. Through the utilization of a multispectral strategy, we were able to capture additional tissues and structures inside the zebrafish. In addition, by employing quantitative reconstruction methods, such as quantitative photoacoustic tomography [29, 30], we can derive the concentrations of different compositions inside the major organs. Although, our study demonstrates the great potential of photoacoustic imaging in the study of adult zebrafish, further improvements must be made to optimize both the imaging system and experimental procedures. First, higher spatial resolution is achievable by the use of ultrasound transducers with a higher center frequency and a shorter focal length [31, 32]. Additionally, the total data collection time (15 minutes for one set of 3D data) can be reduced by the use of pulsed lasers with a high repetition rate and array-based detection units. Finally, the spectral range can be extended to visible and infrared wavelengths.

Acknowledgments

This work was sponsored by National Natural Science Foundation of China (81571722 and 61528401), State International Collaboration Program from Sichuan (2016HH0019), and startup grant (A03012023601011) from University of Electronic Science and Technology of China.